https://doi.org/10.5194/wes-2026-148
Preprint. Discussion started: 18 September 2026
© Author(s) 2026. CC BY 4.0 License.

WIND ENERGY SCIENCE DISCUSSIONS

Simulation-Based Assessment of Flap Scheduling and Operating Height for Ground-Gen Airborne Wind Energy Systems

Pritti Paul[1], Yahya Khurshid[1], Espen Oland[2], Mohamed M. Kamra[1], and Tarek N. Dief[1]

[1]Department of Mechanical and Aerospace Engineering, United Arab Emirates University, Al Ain 15551, UAE
[2]Kitemill AS, 5704 Voss, Norway

Correspondence: Tarek N. Dief (tndief@uaeu.ac.ae)

Abstract. Airborne wind energy systems (AWES) are able to access stronger and more persistent winds at higher operating altitudes, although system performance strongly depends on the choice of aerodynamic actuation, flight-path geometry, and height of operation under realistic wind conditions. In case of rigid-wing ground-generation (ground-gen) AWES, the influence of such a combination of operating parameters on traction-phase performance is still inadequately understood at constant settings of the control algorithms and limitations of the hardware. This paper tries to fill this knowledge gap by studying the impact of several key operating parameters of the ground-gen system with the aid of a validated nonlinear kite–tether–winch simulator of the Kitemill KM1 rigid-wing Ground-Gen AWES. Using a one-factor-at-a-time simulation campaign, the influence of fixed flap deflection, lateral path geometry, wind-field formulation, minimum production height, and elevation angle of the helix axis on the reel-out mechanical power and operation margins was examined. Under the formulation of an altitude-dependent wind field with the time-varying ground-reference wind input, the baseline design produces an average reel-out power of $7.56\,\mathrm{kW}$. Application of speed-scheduled flap deflection in the range of conservative values of $0°$–$10°$ increases the average reel-out power up to $11.10\,\mathrm{kW}$, which corresponds to an increase of around 47% while repeated crosswind operation was maintained in the evaluated simulations. Increasing the minimum production height further improves the average reel-out power to $12.96\,\mathrm{kW}$, which is about 71% above the baseline one. On the other hand, within the tested circle–ellipse comparison, lateral path shape has only a minor influence on average traction power, whereas circular loop radius has a clear effect. Tuning of the elevation angle does not allow increasing the reel-out power further than the minimum height optimization does in the considered operating envelope.

1 Introduction

Airborne wind energy systems (AWES) employ tethered aircraft to access wind resources at operating heights of approximately 300–$1500\,\mathrm{m}$ above ground level, where winds can be stronger and more persistent than closer to the surface (Crismer et al., 2024; Eijkelhof and Schmehl, 2022; Weber et al., 2021). In ground-generation (ground-gen) architectures, the aerodynamic forces developed by the aircraft are transmitted through the tether to a ground-based winch-generator system, where mechanical power is extracted during reel-out and converted into electrical energy (Joshi et al., 2025, 2024). The theoretical basis for crosswind power generation with tethered wings dates back to Loyd (1980), while recent work has highlighted the ongoing

https://doi.org/10.5194/wes-2026-148
Preprint. Discussion started: 18 September 2026
© Author(s) 2026. CC BY 4.0 License.

challenge of achieving reliable autonomous operation under realistic atmospheric conditions (Fagiano et al., 2022). The broader AWES literature also identifies potential advantages such as access to wind resources over a broader range of heights above ground and reduced structural material requirements relative to tower-based systems such as horizontal-axis wind turbines (HAWTs), although the extent of these benefits remains dependent on the system architecture and operating scenario (Malz et al., 2022; Onay et al., 2023; ~~Bošnjaković et al., 2025~~).

Figure ~~Fig.~~ 1 illustrates the pumping-cycle operation of the rigid-wing ground-generation system considered in this study. During the traction phase, the tether is reeled out under high tension while the aircraft follows repeated circular crosswind trajectories, thereby increasing the apparent wind speed and aerodynamic loading (Fagiano et al., 2018; Rapp et al., 2019). During the retraction phase, the aircraft is de-powered, and the tether is reeled in under substantially lower tension. Consequently, the energy consumed during retraction remains smaller than the energy generated during traction, resulting in positive net cycle energy (Rapp et al., 2019; Mohammed et al., 2024b). For all simulations reported here, the VTOL rotors are inactive, such that $\mathbf{F}_R = \mathbf{0}$ and $\mathbf{M}_R = \mathbf{0}$. These terms are retained only to show the general form of the published model.

Although a growing body of work has reported AWES prototypes, control strategies, and simulation frameworks (Khurshid et al., 2025; Vermillion et al., 2021; Fagiano et al., 2022; Marques et al., 2023), there remains limited systematic quantification of how individual operational parameters affect performance under realistic wind conditions when controller settings and hardware limits are held fixed. In the present context, the *flap deflection strategy* refers to the prescribed or scheduled variation of the aerodynamic flap angle, which modifies the lift, drag, and pitching-moment characteristics of the rigid-wing kite ~~rigid wing~~ and therefore affects airspeed, tether tension, reel-out power, and control margin during traction. *Lateral path geometry* denotes the shape of the prescribed crosswind orbit in a local path plane normal to the helix axis. In the baseline case, the traction-phase controller steers the aircraft along a circular orbit of radius R_t.

Motion around this orbit is predominantly crosswind relative to the ambient wind, while simultaneous tether reel-out displaces successive orbits along the helix axis, producing the three-dimensional helical traction trajectory. The *minimum production height* $h_{\min}$ defines the lower bound of the traction loop and therefore determines the altitude band sampled during power generation, which is especially important in vertically sheared wind fields. The *elevation angle* θ_h defines the inclination of the helix axis relative to the ground plane and modifies both the tilt of the trajectory and the distribution of flight time across altitude. Finally, *vertically varying and time-varying wind fields* alter the apparent wind speed, dynamic pressure, tether loading, and force-tracking response of the winch, thereby influencing both traction power and flight stability. The combined influence of these factors has not been sufficiently characterized for rigid-wing ground-gen systems under a common controller and fixed hardware constraints.

This work addresses that gap using the nonlinear kite–tether–winch simulator of the KM1 platform described and assessed against flight data by Mohammed et al. (2024a). ~~As shown in Fig. 2,~~ the KM1 prototype shown in Fig. 2 has been deployed and operated in field conditions, providing a practical reference for the hardware configuration, operating envelope, and safety constraints represented in the simulation model. A common baseline controller and fixed hardware and safety constraints are retained across all simulation cases so that the observed performance differences can be attributed to operational choices rather than controller retuning. Within this framework, the study examines constant flap settings, flight-path geometries, and wind-field

https://doi.org/10.5194/wes-2026-148
Preprint. Discussion started: 18 September 2026
© Author(s) 2026. CC BY 4.0 License.

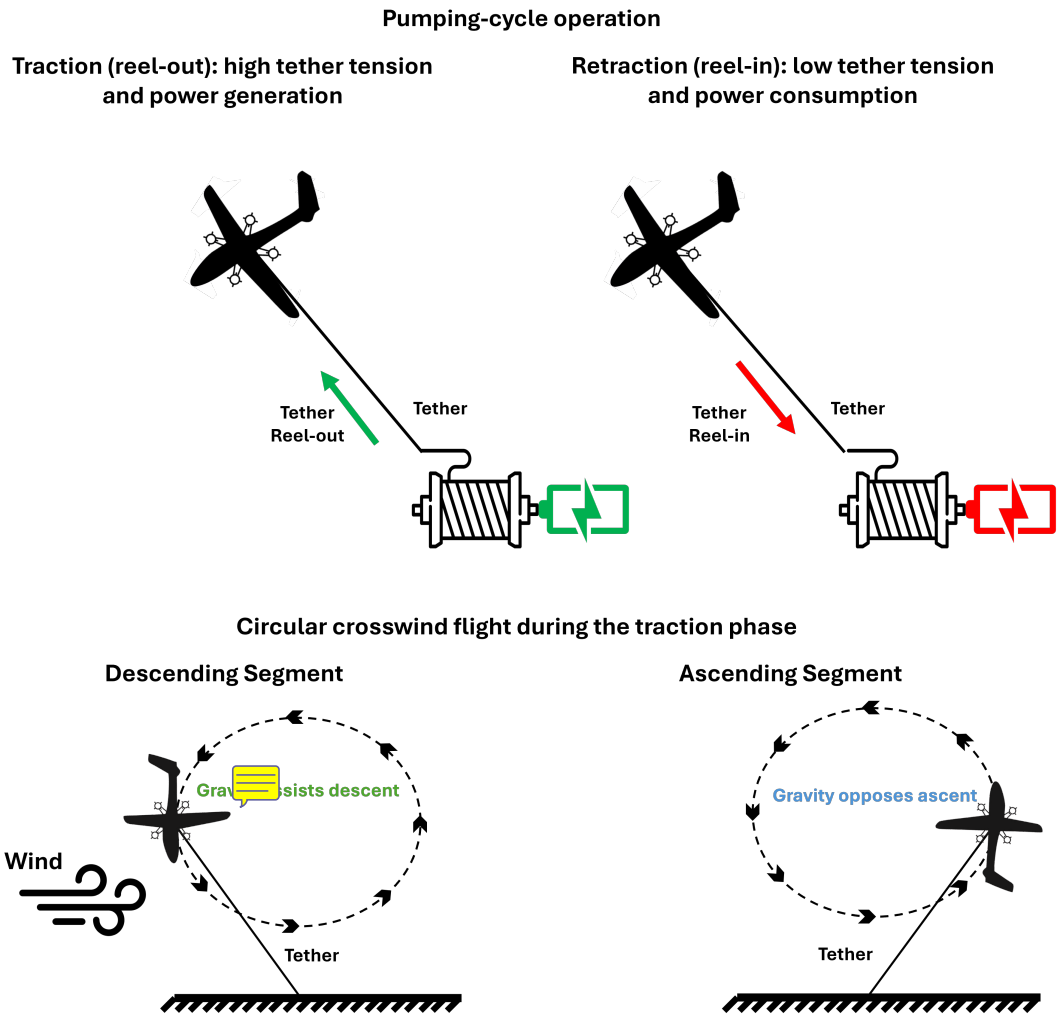

Figure 1. Conceptual illustration of the operating sequence of a ~~single~~ rigid-wing ground-generation airborne wind energy system. The upper panel shows pumping-cycle operation: the tether is reeled out at high tension during the traction phase to generate electrical power and reeled in at low tension during the retraction phase, which consumes part of the generated energy. The lower panel details circular crosswind flight during the traction phase, separating the descending and ascending segments. All aircraft drawings represent the same aircraft at successive instants. Dashed arrows around the circular paths indicate aircraft flight direction, whereas the solid coloured arrows along the tether indicate reel-out or reel-in motion; ~~none represents a force vector. The VTOL rotors are inactive during the illustrated pumping-cycle phases.~~

representations, and further evaluates speed-scheduled flap actuation together with changes in minimum production height and elevation angle. The objective is to quantify their effect on average reel-out mechanical power and operating margins for the KM1 system under variable wind conditions.

The remainder of the paper is organized as follows. Section ~~Sect.~~ 2 presents the dynamic model and simulation framework. Section ~~Sect.~~ 3 describes the simulation methodology, including the reference operating condition, investigated cases, and performance met-

https://doi.org/10.5194/wes-2026-148
Preprint. Discussion started: 18 September 2026
© Author(s) 2026. CC BY 4.0 License.

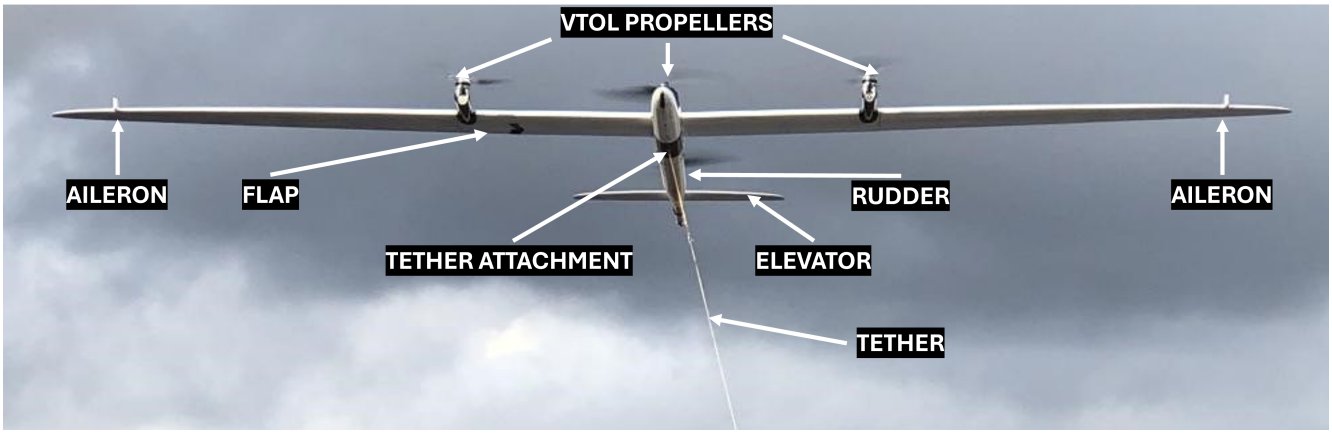

Figure 2. Field operation of the KM1 prototype, illustrating the kite–tether–winch configuration used as the physical reference for the nonlinear simulation model.

rics. Section ~~Sect.~~ 4 reports the simulation results for the investigated operating parameters. Section ~~Sect.~~ 5 discusses the main findings, their relation to prior AWES studies, and the limitations of the present work. Section ~~Sect.~~ 6 summarizes the principal conclusions. Appendix A summarizes the KM1 parameters, operating limits, and study-specific settings used in the simulation campaign.

2 Dynamic model and simulation framework

This study employs the nonlinear kite–tether–winch simulator of the Kitemill KM1 rigid-wing ground-gen AWES ~~airborne wind energy system~~ described by Mohammed et al. (2024a). The simulator comprises a six-degree-of-freedom rigid-wing aircraft model, a deformable tether model, and a speed-controlled ground-station winch, corresponding to the physical KM1 configuration shown in Fig. 2. The dynamic and aerodynamic model was assessed against KM1 flight data by Mohammed et al. (2024a), while the traction-phase flight-control architecture for circular crosswind operation is described by Mohammed et al. (2024b). The present work does not introduce a new dynamic model; rather, it applies the published model and control framework to quantify how selected operating parameters influence system performance. Appendix A summarizes the platform parameters, operating limits, and study-specific settings used in the present simulation campaign.

2.1 Reference frames and state variables

A right-handed body-fixed frame (x_b, y_b, z_b) is attached to the aircraft, with x_b directed along the fuselage, y_b toward the right wing tip, and z_b downward. An inertial wind frame $A = (X, Y, Z)$ is anchored at the ground station, with X aligned with the prevailing wind and Z directed downward. The reference-frame definitions and aircraft-state notation follow Mohammed et al. (2024a). The aircraft's position in the inertial frame is written as

$$\mathbf{p}_k = \begin{bmatrix} p_X & p_Y & p_Z \end{bmatrix}^{\mathsf{T}}, \tag{1}$$

https://doi.org/10.5194/wes-2026-148
Preprint. Discussion started: 18 September 2026
© Author(s) 2026. CC BY 4.0 License.

and the altitude is

$$h = -p_Z. \tag{2}$$

The aircraft state is described by the body-fixed translational velocity vector,

$$\mathbf{v}_b = \begin{bmatrix} U & V & W \end{bmatrix}^\mathsf{T}, \tag{3}$$

the attitude quaternion,

$$\mathbf{q} = \begin{bmatrix} q_0 & q_1 & q_2 & q_3 \end{bmatrix}^\mathsf{T}, \tag{4}$$

and the body angular velocity vector,

$$\boldsymbol{\omega}_b = \begin{bmatrix} p & q & r \end{bmatrix}^\mathsf{T}. \tag{5}$$

The complete simulator state additionally includes the tether nodal positions and velocities, the winch speed, and the paid-out tether length.

2.2 Winch model

Following Mohammed et al. (2024a), the ground-station winch is represented as a first-order speed-controlled system. Its reel-out speed v_t evolves according to

$$\dot{v}_t = \frac{v_t^{\mathrm{ref}} - v_t}{\tau_w}, \tag{6}$$

where v_t^{ref} is the commanded reel speed and τ_w is the winch time constant. The tether length evolves as

$$\dot{\ell}_t = v_t. \tag{7}$$

During traction, the reference reel speed is generated by a force-tracking law based on the measured ground-station tether tension, such that the winch reels out when the measured load exceeds the reference value and reels in when it falls below that value. The instantaneous mechanical power at the drum is computed as

$$P_w(t) = F_{t,\mathrm{GS}}(t)\, v_t(t), \tag{8}$$

where $F_{t,\mathrm{GS}}$ denotes the scalar tether tension at the ground station. With this sign convention, $P_w > 0$ during reel-out and $P_w < 0$ during reel-in. The corresponding accumulated energy is given by

$$E_w(t) = \int_0^t P_w(\tau)\, \mathrm{d}\tau. \tag{9}$$

2.3 Tether model

The lumped-mass tether formulation follows Mohammed et al. (2024a). The tether is represented as a chain with N_t internal nodes connected by tension-only spring–damper elements. This formulation allows the tether to carry tensile loads while

https://doi.org/10.5194/wes-2026-148
Preprint. Discussion started: 18 September 2026
© Author(s) 2026. CC BY 4.0 License.

preventing nonphysical compressive forces. Each tether element is subjected to gravity and aerodynamic drag, and the tether dynamics are solved simultaneously with the aircraft and winch dynamics. The ground-station end of the tether is fixed at the winch, whereas the airborne end is kinematically constrained to the tether attachment point on the aircraft. The effective axial stiffness varies with the instantaneous paid-out tether length. In compact form, the length-dependent stiffness is represented by

$$K_t = \frac{\bar{F}_t}{\bar{\epsilon}_t \, \ell_t}, \tag{10}$$

where $\bar{F}_t$ and $\bar{\epsilon}_t$ denote the tether breaking load and the elongation at that load, respectively. The complete node-level tether formulation, including the elastic, damping, gravitational, and aerodynamic drag terms, is reported by Mohammed et al. (2024a) and is not repeated here.

2.4 Aircraft dynamics and aerodynamic model

The six-degree-of-freedom aircraft model, including the aerodynamic, tether, and gravitational force and moment contributions, follows Mohammed et al. (2024a). The full simulator also contains rotor-force and rotor-moment channels whose use for fault-tolerant traction-phase control is described by Mohammed et al. (2024b).

The apparent-wind velocity vector is expressed in the body-fixed frame as $\mathbf{v}_a = [v_{a,x} \; v_{a,y} \; v_{a,z}]^\mathsf{T}$, where $v_{a,x}$, $v_{a,y}$, and $v_{a,z}$ are its components along the x_b, y_b, and z_b axes, respectively. Its magnitude defines the aircraft airspeed:

$$V_a = \|\mathbf{v}_a\|_2 = \sqrt{v_{a,x}^2 + v_{a,y}^2 + v_{a,z}^2}, \tag{11}$$

where the subscript 2 denotes the Euclidean norm.

The angle of attack α and sideslip angle β are calculated from the same body-fixed apparent-wind components as

$$\alpha = \operatorname{atan2}(v_{a,z}, v_{a,x}), \tag{12}$$

and

$$\beta = \arcsin\left(\frac{v_{a,y}}{V_a}\right). \tag{13}$$

The aerodynamic forces are obtained from

$$F_D = q_\infty S C_D, \qquad F_Y = q_\infty S C_Y, \qquad F_L = q_\infty S C_L, \tag{14}$$

where S is the wing area and q_∞ is the dynamic pressure, defined as

$$q_\infty = \frac{1}{2}\rho(h) V_a^2, \tag{15}$$

where $\rho(h)$ is the air density at altitude h. The corresponding aerodynamic moments are

$$M_{Ax} = q_\infty S b C_l, \qquad M_{Ay} = q_\infty S \bar{c} C_m, \qquad M_{Az} = q_\infty S b C_n, \tag{16}$$

https://doi.org/10.5194/wes-2026-148
Preprint. Discussion started: 18 September 2026
© Author(s) 2026. CC BY 4.0 License.

where b is the wingspan and $\bar{c}$ is the mean aerodynamic chord. The aerodynamic coefficient model follows the CFD-based KM1 formulation reported by Mohammed et al. (2024a), namely

$$C_D = C_{D,0} + \Delta C_D(\alpha, \beta, \delta_f), \tag{17}$$

$$C_Y = \Delta C_Y(\alpha, \beta, \delta_r) + C_{Y_p}\frac{pb}{2V_a} + C_{Y_r}\frac{rb}{2V_a}, \tag{18}$$

$$C_L = C_{L,0} + \Delta C_L(\alpha, \delta_f, \beta, \delta_e, \delta_a) + C_{L_q}\frac{q\bar{c}}{2V_a}, \tag{19}$$

$$C_l = \Delta C_l(\alpha, \beta, \delta_a, \delta_r) + C_{l_p}\frac{pb}{2V_a} + C_{l_r}\frac{rb}{2V_a}, \tag{20}$$

$$C_m = \Delta C_m(\alpha, \delta_f, \delta_e, \delta_a) + C_{m_q}\frac{q\bar{c}}{2V_a}, \tag{21}$$

$$C_n = \Delta C_n(\beta, \delta_a, \delta_r) + C_{n_p}\frac{pb}{2V_a} + C_{n_r}\frac{rb}{2V_a}. \tag{22}$$

The complete polynomial coefficient functions, numerical coefficient values, and supporting aerodynamic plots are not reproduced here. The translational rigid-body dynamics may be written compactly as

$$m_a\dot{\mathbf{v}}_b = \mathbf{F}_A + \mathbf{F}_t + \mathbf{F}_R + m_a\mathbf{g}_b - \boldsymbol{\omega}_b \times (m_a\mathbf{v}_b), \tag{23}$$

where $\mathbf{F}_A$, $\mathbf{F}_t$, and $\mathbf{F}_R$ denote the aerodynamic, tether, and rotor-force contributions, respectively, and $\mathbf{g}_b$ is the gravity vector resolved in the body frame. The tether does not act through the aircraft's center of gravity; therefore, it generates the moment

$$\mathbf{M}_t = \mathbf{r}_{t/CG} \times \mathbf{F}_t, \tag{24}$$

where $\mathbf{r}_{t/CG}$ is the vector from the center of gravity to the tether attachment point. The rotational dynamics are written as

$$\mathbf{J}\dot{\boldsymbol{\omega}}_b + \boldsymbol{\omega}_b \times (\mathbf{J}\boldsymbol{\omega}_b) = \mathbf{M}_A + \mathbf{M}_t + \mathbf{M}_R, \tag{25}$$

where $\mathbf{J}$ is the aircraft inertia matrix, and $\mathbf{M}_A$ and $\mathbf{M}_R$ denote aerodynamic and rotor-generated moments, respectively. Quaternion kinematics are used for attitude propagation in order to avoid the singularities associated with Euler-angle representations.

2.5 Guidance and wind-field representation

During traction, the aircraft is commanded to follow a prescribed orbit defined in the traction-frame plane normal to the helix axis, while the winch regulates tether tension through force tracking. Motion around the orbit is predominantly crosswind relative to the ambient wind. As the tether reels out, successive orbits are displaced along the helix axis, producing a three-dimensional helical trajectory. The traction-phase flight-control architecture, including the use of rudder actuation to maintain

https://doi.org/10.5194/wes-2026-148
Preprint. Discussion started: 18 September 2026
© Author(s) 2026. CC BY 4.0 License.

circular crosswind loops, follows Mohammed et al. (2024b). The wind field is applied both at the aircraft and along the tether. Depending on the simulation case, the inflow is represented as a uniform freestream, an altitude-dependent wind profile, or an altitude-dependent profile combined with a time-varying ground-reference wind speed.

In this study, the term altitude-dependent wind field refers to vertical wind shear, i.e., the variation of horizontal wind speed with height above the ground. The altitude-dependent wind field is represented using a logarithmic vertical wind profile. The horizontal wind speed at altitude h is defined as

$$v_w(h) = \begin{cases} v_1, & h < h_1, \\ v_1 \dfrac{\ln(h/z_0)}{\ln(h_1/z_0)}, & h \geq h_1, \end{cases} \tag{26}$$

where h is the altitude above ground, $v_w(h)$ is the horizontal wind speed at altitude h, h_1 is the reference height, v_1 is the wind speed at the reference height, and z_0 is the terrain roughness length.

In the height-dependent wind cases, the parameters are selected as

$$h_1 = 10\ \mathrm{m}, \qquad v_1 = 9\ \mathrm{m\,s^{-1}}, \qquad z_0 = 0.03\ \mathrm{m}. \tag{27}$$

The reference height $h_1 = 10\ \mathrm{m}$ specifies the altitude at which the reference wind speed $v_1 = 9\ \mathrm{m\,s^{-1}}$ is defined; it does not represent the upper limit of the wind field. The logarithmic profile is evaluated at the instantaneous aircraft altitude $h(t)$ and at the local height of each tether element. Fig. 5 presents the profile over the plotted altitude range of 0–$600\ \mathrm{m}$.

The value $z_0 = 0.03\ \mathrm{m}$ represents generic open grassland or agricultural terrain with few obstacles; it is not a site-specific roughness estimate. In the time-varying ground-wind cases, the reference speed v_1 in Eq. (26) is replaced by the prescribed ground-reference wind signal, so that the temporal variation is propagated through the same vertical shear profile. This common dynamic framework is used throughout the study so that performance differences can be attributed to operational choices rather than to changes in model structure.

3 Simulation methodology

The validated dynamic model described in Sect. 2 is used to quantify how selected operational parameters affect traction-phase performance and flight stability under fixed hardware and control constraints. The study is designed as a one-factor-at-a-time simulation campaign, with all non-investigated parameters retained at their reference values. Each case is simulated over multiple pumping cycles, and reel-out and reel-in intervals are identified by the sign of the winch speed so that the reported quantities can be averaged both phase-wise and over complete cycles.

3.1 Validation basis and parameter set

The simulator configuration adopted here, including the winch, tether, aircraft, and aerodynamic models, is based on the KM1 framework described and compared with Kitemill flight data by Mohammed et al. (2024a). The traction-phase flight-controller

https://doi.org/10.5194/wes-2026-148
Preprint. Discussion started: 18 September 2026
© Author(s) 2026. CC BY 4.0 License.

structure follows Mohammed et al. (2024b). The present work, therefore, uses an already validated simulator and controller configuration rather than re-identifying model parameters. The KM1 platform parameters, actuator limits, winch properties, tether limits, and study-specific settings are summarized in Appendix A, allowing the main methodology section to focus on the simulation design and investigated operating cases.

3.2 Reference operating condition

Unless stated otherwise, the reference operating condition is defined by a minimum production height of $150\ \mathrm{m}$, a helix-axis elevation angle of $10°$, and a flap deflection of $5°$. These values define the common geometric and control baseline used throughout the comparative study. It should be noted that the prescribed quantity is the helix-axis elevation angle, not a fixed aircraft elevation, because the aircraft follows a periodic crosswind trajectory rather than remaining at a constant altitude.

For the geometry and constant-flap sensitivity studies, a uniform freestream wind speed of $12\ \mathrm{m\,s^{-1}}$ is used in order to isolate the effect of the investigated operating parameter. For the variable-wind studies and the progressive optimization sequence, the reference inflow combines an altitude-dependent wind profile with a time-varying ground-reference wind signal, consistent with the conditions used in the results section.

3.3 Investigated simulation cases

The simulation campaign examines five classes of operating variation. First, constant flap-deflection sweeps are used to quantify the trade-off between airspeed, tether tension, and mechanical power, and to identify stability limits under fixed control settings. Second, the prescribed lateral path geometry is varied by comparing circular and elliptical trajectories and by changing the circular path radius. Third, the inflow model is changed from a uniform freestream to an altitude-dependent wind profile and then to an altitude-dependent profile with time-varying ground-reference wind speed. Fourth, the minimum production height is varied in order to assess how the sampled altitude band affects traction power. Fifth, the helix-axis elevation angle is varied to examine the trade-off between time spent in stronger winds aloft and the corresponding changes in flight kinematics and operating margins.

In all cases, the same controller structure, actuator limits, winch limits, and hardware parameters are retained. Consequently, the resulting performance differences can be attributed to the investigated operating variable rather than to controller retuning or changes in system hardware.

3.4 Performance metrics

The primary performance metric is the mean mechanical power at the ground-station drum during reel-out. Instantaneous mechanical power is calculated from Eq. (8), and the average reel-out power is defined as

$$\bar{P}_{\mathrm{out}} = \frac{1}{T_{\mathrm{out}}} \int\limits_{v_t>0} P_w(t)\,\mathrm{d}t, \tag{28}$$

https://doi.org/10.5194/wes-2026-148
Preprint. Discussion started: 18 September 2026
© Author(s) 2026. CC BY 4.0 License.

Table 1. Summary of representative reel-out power results for the investigated cases.

Case	Average reel-out power (kW)
Height-dependent wind only	8.36
Time-varying ground wind with height-dependent profile (baseline case)	7.56
Adaptive flap scheduling	11.10
Optimized minimum production height	12.96
Optimized elevation angle	12.96

where T_{out} denotes the cumulative duration of the reel-out intervals. The net energy over a complete pumping cycle is

$$E_{\mathrm{cyc}} = \int_0^{T_{\mathrm{cyc}}} P_w(t)\,\mathrm{d}t, \tag{29}$$

where T_{cyc} is the cycle duration.

In addition to the power metrics, the analysis tracks aircraft airspeed, altitude, reel speed, and ground-station tether tension in order to assess whether each operating condition remains within the relevant flight and hardware limits. The comparison of all cases is therefore based not only on power output, but also on the corresponding operating margins and qualitative flight stability.

4 Results

This section reports the simulation outputs for the investigated operating parameters. The common reference condition described in Sect. 3 is used as the baseline for comparison throughout this section, except where a different baseline is explicitly identified. Table 1 summarizes the principal reel-out power values obtained for the wind-field and optimization cases.

4.1 Constant flap deflection during traction

Four fixed flap settings, $\delta_f \in \{0°, 5°, 10°, 15°\}$, were simulated under the reference operating condition. Fig. 3 shows the corresponding variation in aircraft airspeed and average reel-out mechanical power. As the flap deflection increased, the airspeed decreased monotonically. Over the same range, the average reel-out power increased from the zero-flap case to the moderate-flap cases and then deteriorated as the fixed-flap condition approached the boundary of stable operation. Repeated stable operation was maintained at low and moderate flap deflections, whereas the largest tested flap settings were associated with tension collapse and descent episodes. The $15°$ case did not produce a stable periodic solution and is therefore not included in the averaged data shown in Fig. 3.

https://doi.org/10.5194/wes-2026-148
Preprint. Discussion started: 18 September 2026
© Author(s) 2026. CC BY 4.0 License.

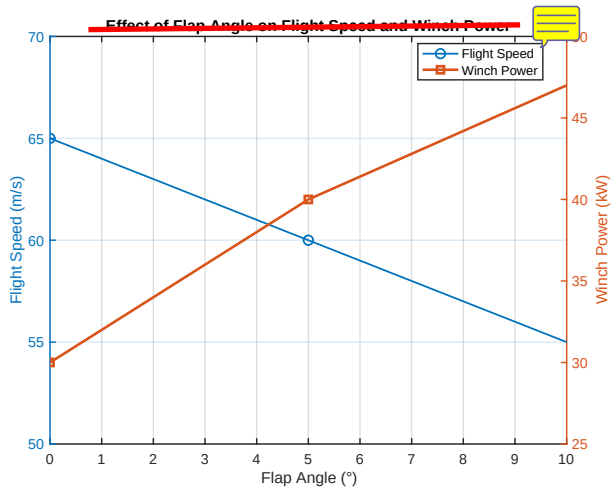

Figure 3. Effect of constant flap deflection on aircraft airspeed and average reel-out mechanical power.

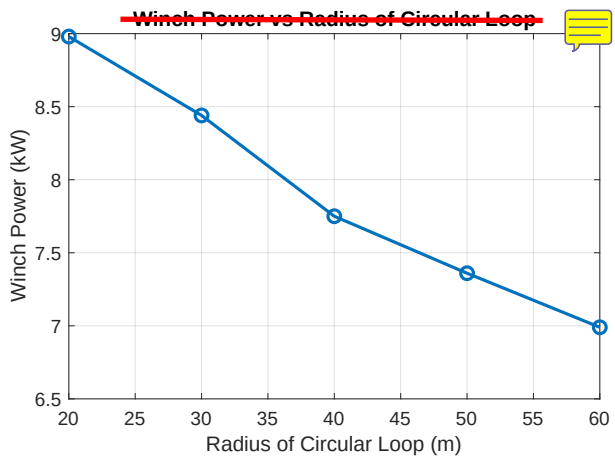

Figure 4. Average reel-out mechanical power as a function of circular loop radius.

4.2 Flight-path geometry

The effect of lateral path geometry was assessed by comparing circular and elliptical trajectories and by varying the circular path radius. Figure ~~Fig.~~ 4 shows the dependence of average reel-out mechanical power on circular loop radius. For circular paths, the average reel-out mechanical power decreased from $8.98\ \mathrm{kW}$ at a radius of $20\ \mathrm{m}$ to $6.99\ \mathrm{kW}$ at a radius of $60\ \mathrm{m}$. Replacing the circular path with an elliptical trajectory produced only minor changes in average reel-out mechanical power under the tested conditions.

https://doi.org/10.5194/wes-2026-148
Preprint. Discussion started: 18 September 2026
© Author(s) 2026. CC BY 4.0 License.

4.3 Wind-field cases

4.3.1 Height-dependent wind

The height-dependent wind case uses the logarithmic vertical shear profile defined in Eq. (26), with the parameters listed in Eq. (27). The $10\ \mathrm{m}$ level is used as the near-surface reference height, while the prescribed value $v_1 = 9\ \mathrm{ms^{-1}}$ produces a strong sensitivity case. The roughness length $z_0 = 0.03\ \mathrm{m}$ represents generic open grassland or agricultural terrain. The profile is displayed up to $600\ \mathrm{m}$, consistent with the maximum modelled tether length reported in Table A2; this upper plotting limit does not imply that the aircraft operates at an altitude of $600\ \mathrm{m}$.

Because the adopted formulation is logarithmic rather than a power-law profile, it is characterised by z_0 and does not use a shear exponent. The implemented profile is constant below h_1 and increases logarithmically above it. For this controlled sensitivity study, it provides an idealised open-terrain inflow with which to examine how the altitude band sampled during traction affects system performance. ~~Eq.~~ Equation (26) gives $v_w(100\ \mathrm{m}) = 12.57\ \mathrm{ms^{-1}}$ and $v_w(600\ \mathrm{m}) = 15.34\ \mathrm{ms^{-1}}$. The extension of the logarithmic law to $600\ \mathrm{m}$ is an idealised extrapolation, and the resulting profile is favourable for energy production. The reported absolute power level is therefore conditional on this prescribed inflow.

Simple logarithmic profiles are useful as controlled AWES reference cases but cannot represent the complete temporal and vertical variability of site-specific winds (Sommerfeld et al., 2023). This distinction is particularly relevant at Lista, which Cheynet et al. (2025) classify as a coastal site. They describe the coastal sites considered in their study as being affected by sharp roughness transitions from open water to flat agricultural terrain, which can generate internal boundary layers. A stationary logarithmic profile with one roughness length should therefore not be interpreted as a reconstruction of the Lista wind climate. A site-specific energy-yield assessment would require measured or validated time-varying profiles together with long-term wind statistics.

The resulting vertical wind-speed profile is shown in Fig. 5. Under this inflow, the simulator produced an average reel-out mechanical power of approximately $8.36\ \mathrm{kW}$. The corresponding ground-station mechanical-power trace is shown in Fig. 6. It exhibits systematic modulation over the crosswind loop and brief negative-power intervals associated with corrective reel-in actions within the nominal traction interval. Consistent with Eq. (28), the reported average reel-out power includes only samples for which $v_t > 0$.

4.3.2 Time-varying reference-height wind

To examine the response of the coupled aircraft–tether–winch system and its fixed flight and winch controllers to a slowly varying but repeatable inflow, the wind speed at the $10\ \mathrm{m}$ reference height was prescribed as

$$v_1(t) = \bar{v}_1 + A_v \sin\left(\frac{2\pi t}{T_v}\right), \tag{30}$$

where $\bar{v}_1 = 8\ \mathrm{ms^{-1}}$, $A_v = 1\ \mathrm{ms^{-1}}$, and $T_v = 600\ \mathrm{s}$.

The $1\ \mathrm{ms^{-1}}$ amplitude provides a moderate, bounded variation of $\pm 12.5\,\%$ about the mean while retaining the reference-height wind speed within 7–9 $\mathrm{ms^{-1}}$. The single-frequency form provides a deterministic and repeatable sensitivity input, al-

https://doi.org/10.5194/wes-2026-148
Preprint. Discussion started: 18 September 2026
© Author(s) 2026. CC BY 4.0 License.

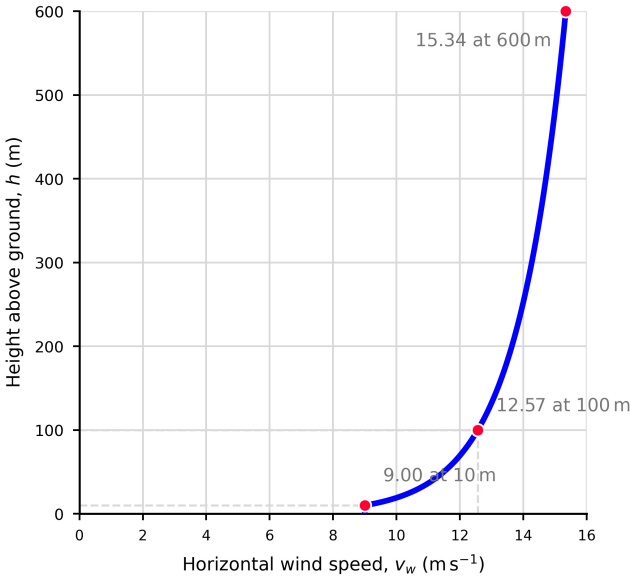

Figure 5. Imposed logarithmic vertical wind-speed profile used for the height-dependent sensitivity case. The parameters $v_1 = 9\ \mathrm{m\,s^{-1}}$ at $h_1 = 10\ \mathrm{m}$ and $z_0 = 0.03\ \mathrm{m}$ give $v_w(100\ \mathrm{m}) = 12.57\ \mathrm{m\,s^{-1}}$ and $v_w(600\ \mathrm{m}) = 15.34\ \mathrm{m\,s^{-1}}$. This strong, idealised open-terrain profile was not fitted to observations at Lista.

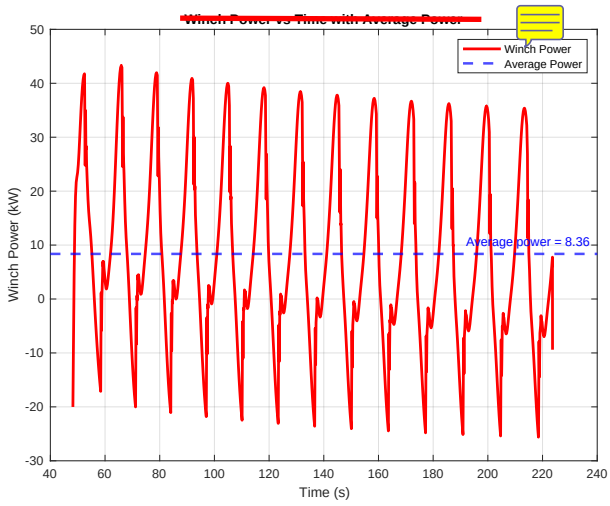

Figure 6. Ground-station mechanical-power trace over the nominal traction interval for the height-dependent wind case. The reported average reel-out power includes only samples for which $v_t > 0$.

lowing the controller response to increasing and decreasing reference wind speed to be examined without introducing stochastic variability. Its 600 s period is long relative to the repeated crosswind-loop oscillations in the traction-power response and there-

https://doi.org/10.5194/wes-2026-148
Preprint. Discussion started: 18 September 2026
© Author(s) 2026. CC BY 4.0 License.

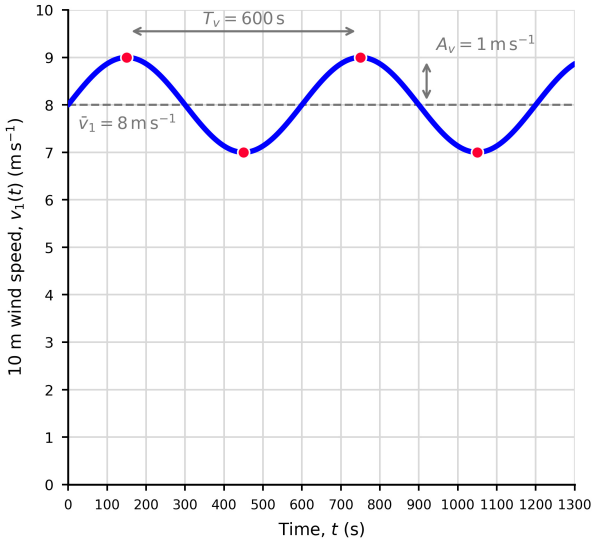

Figure 7. Prescribed deterministic variation of the 10 m reference wind speed $v_1(t)$, with a mean of $8\ \mathrm{m\,s^{-1}}$, an amplitude of $1\ \mathrm{m\,s^{-1}}$, and a period of 600 s. The signal is an idealised sensitivity input rather than a measured Lista wind record or a model of atmospheric turbulence.

fore represents a slowly varying background inflow rather than a loop-scale disturbance. The signal was not derived from measurements at Lista and is not intended to represent atmospheric turbulence, a gust spectrum, or a site-specific wind record.

The prescribed reference-height signal is shown in Fig. 7. The corresponding wind field at the aircraft and along the tether is computed using the wind-field formulation described in Sect. 2.5.

Under this prescribed inflow, the average reel-out mechanical power was 7.56 kW, and the corresponding mechanical-power trace is shown in Fig. 8. Because the steady height-dependent case uses $v_1 = 9\ \mathrm{m\,s^{-1}}$, whereas the time-varying case has a mean reference speed of $8\ \mathrm{m\,s^{-1}}$, the difference between the two reported average-power values reflects both the lower mean reference wind speed and the imposed temporal variation. This comparison therefore cannot isolate the effect of wind unsteadiness.

4.4 Adaptive flap scheduling

A speed-scheduled flap law was introduced to adapt the aerodynamic loading of the aircraft to the changing speed condition along the traction trajectory while retaining the baseline path-following and winch-control structures. A single fixed flap setting represents a compromise between increasing aerodynamic loading and preserving sufficient aircraft speed and control margin.

Flap deflection modifies the lift, drag, and pitching-moment coefficient functions of the KM1 aerodynamic model and consequently affects aircraft airspeed, tether tension, trim demand, and winch response. A larger flap command can increase aerodynamic loading and thereby potentially increase tether tension. However, the accompanying increase in drag and pitch-trim demand can reduce aircraft speed and control margin. The schedule is therefore intended to apply the larger command when the speed condition permits additional loading and to return towards the nominal setting as the speed condition decreases.

https://doi.org/10.5194/wes-2026-148
Preprint. Discussion started: 18 September 2026
© Author(s) 2026. CC BY 4.0 License.

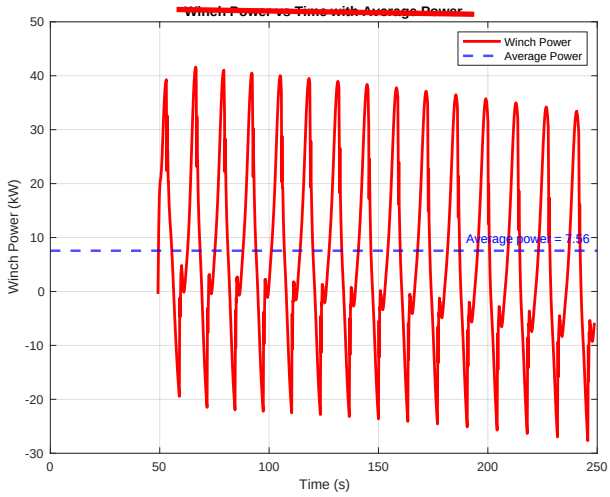

Figure 8. Ground-station mechanical-power trace over the nominal traction interval for the time-varying reference-wind case. The reported average reel-out power includes only samples for which $v_t > 0$.

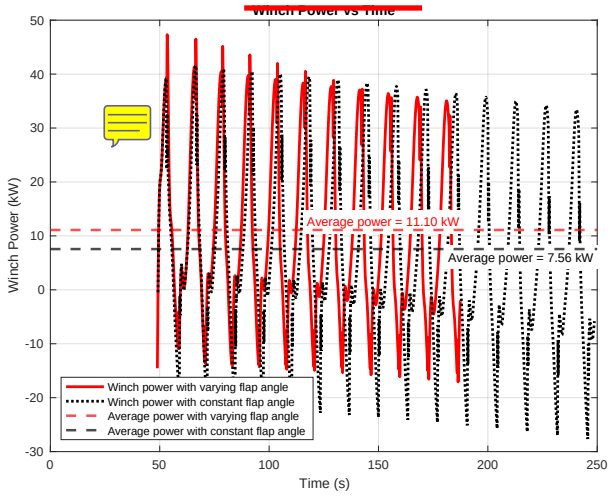

Figure 9. Comparison of winch-power traces for the constant-flap baseline and the speed-scheduled flap case. The average reel-out power increases from 7.56 kW for the constant-flap case to 11.10 kW with flap modulation.

Because the ground-station mechanical power is $P_w = F_{t,\mathrm{GS}} v_t$, the resulting power increase should be interpreted as the coupled response of the aircraft–tether–winch system rather than as an isolated increase in lift. The fixed-flap sweep in Sect. 4.1 provided the basis for the scheduling limits. The 5° and 10° cases retained repeated operation, whereas the 15° case did not reach stable periodic operation. Accordingly, 10° was retained as a conservative upper command limit.

Figure ~~Fig.~~ 9 compares the winch-power response obtained with the constant-flap baseline and with speed-scheduled flap modulation. Under the same variable-wind simulation framework, the scheduled-flap case increased the average reel-out power from

https://doi.org/10.5194/wes-2026-148
Preprint. Discussion started: 18 September 2026
© Author(s) 2026. CC BY 4.0 License.

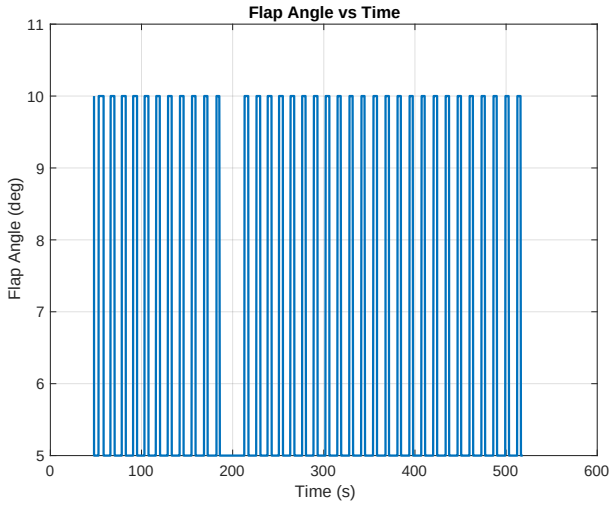

Figure 10. Commanded flap setpoint $\delta_{f,\mathrm{cmd}}$ generated by the speed-dependent scheduling logic.

7.56 to 11.10 kW. The scheduling law generates a commanded flap setpoint, $\delta_{f,\mathrm{cmd}}$, subject to the prescribed $0°$–$10°$ saturation range. Over the interval displayed in Fig. 10, the command alternates between the nominal $5°$ setting and the $10°$ upper setting. The plotted quantity is a controller command and should not be interpreted as a measured flap position, servo-feedback signal, or instantaneous physical flap motion. The physical control-surface response is represented separately by the first-order actuator model described in Sect. A2.

The piecewise-constant form of the command reflects the bounded implementation of the scheduling law, in which the setpoint is updated according to the estimated speed condition and clipped within the prescribed operating range. With the speed-scheduled flap active, the corresponding reeling-out power trace is shown in Fig. 11. No orbit loss was observed over the simulated cases with the imposed scheduling limits, indicating that the flap schedule increased traction-phase power while preserving the repeated crosswind operation of the KM1 model.

4.5 Minimum production height

This variation was introduced to determine whether raising the lower boundary of the traction trajectory shifts the complete loop into a more favourable altitude band under the prescribed vertical wind shear. The reference value was $h_{\min} = 150$ m. The path geometry, controller structure, and hardware limits were retained so that the comparison reflects the influence of the sampled altitude band rather than controller retuning. The investigated values constitute a model-based sensitivity study and are not intended as a site-specific operating-height or airspace recommendation for Lista.

The available simulations indicated a best-performing region around 200–220 m, with the highest reported average reel-out power, approximately 12.96 kW, obtained near 200 m. Accordingly, this value is referred to as the best-performing evaluated setting rather than as a universally optimal production height. The corresponding reel-out power trace is shown in Fig. 12.

https://doi.org/10.5194/wes-2026-148
Preprint. Discussion started: 18 September 2026
© Author(s) 2026. CC BY 4.0 License.

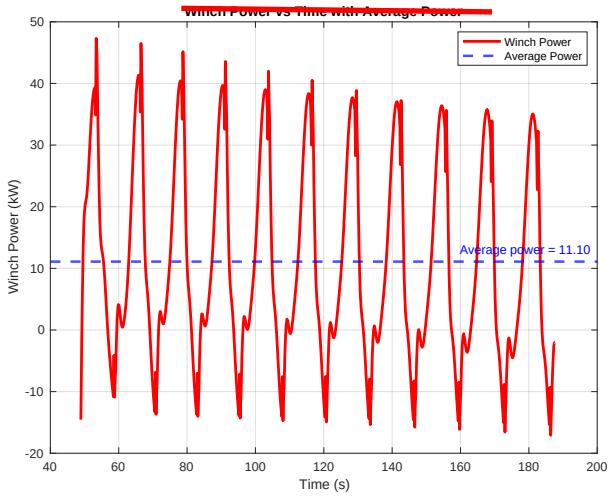

Figure 11. Reeling-out power trace for the adaptive flap-scheduling case.

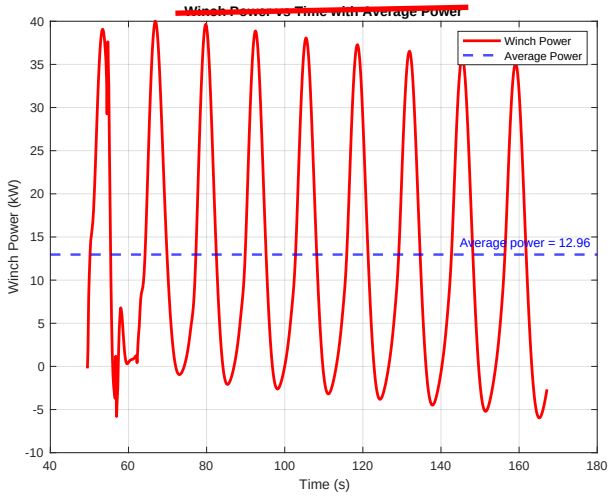

Figure 12. Reeling-out power trace for the minimum-production-height optimum.

4.6 Elevation angle

The helix-axis elevation angle was varied after selecting the minimum-production-height setting to determine whether changing the inclination and altitude distribution of the trajectory could provide an additional power benefit. During this sequential sensitivity test, the selected minimum height, controller structure, and hardware limits were retained. Unlike changing $h_{\min}$, which translates the lower boundary of the trajectory, changing θ_h alters the inclination and flight kinematics of the helical path. The investigated angles should therefore be interpreted as controller-specific sensitivity cases rather than as a general or site-specific optimization.

https://doi.org/10.5194/wes-2026-148
Preprint. Discussion started: 18 September 2026
© Author(s) 2026. CC BY 4.0 License.

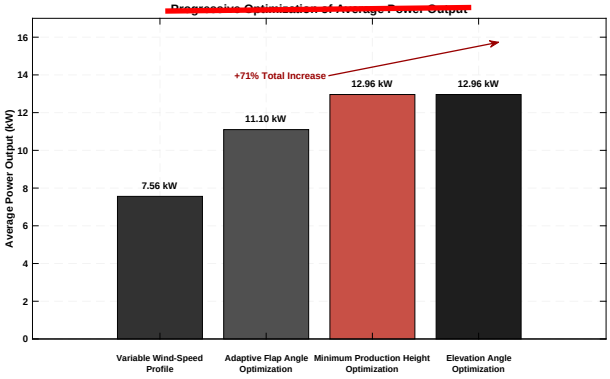

Figure 13. Progressive optimization of average reel-out power.

Among the evaluated cases, the best-performing setting was $\theta_h = 10°$, for which the average reel-out power was 12.96 kW. This matched the result obtained after minimum-height selection and therefore provided no additional improvement. Because the elevation-angle case produced the same average reel-out power, a separate power trace is not repeated here.

5 Discussion

5.1 Aerodynamic actuation and traction stability

The fixed-flap sweep demonstrates that aerodynamic actuation affects traction power through coupled changes in aircraft speed, aerodynamic loading, tether tension, and winch response. Because the ground-station mechanical power is $P_w = F_{t,\mathrm{GS}} v_t$, a reduction in aircraft airspeed does not necessarily produce a reduction in reel-out power. Over the low-to-moderate deflection range, flap deflection increased the product of tether tension and reel-out speed even though the aircraft airspeed decreased. The available simulation outputs do not isolate the individual contributions of lift, drag, pitching moment, tether loading, and force-controlled winch response; therefore, the observed improvement should be interpreted as the coupled response of the aircraft–tether–winch system.

This favorable trend did not continue indefinitely. The largest fixed flap deflections were associated with tension collapse and aircraft descent, and the $15°$ case did not reach stable periodic operation. This behavior indicates that the power improvement is bounded by the available aerodynamic and control margins, although the present results do not uniquely identify the mechanism that initiates the loss of periodic operation.

Under the same variable-wind framework, speed-scheduled flap actuation increased the average reel-out power from 7.56 to 11.10 kW. Bounding the commanded flap deflection between $0°$ and $10°$ allowed the schedule to modify aerodynamic loading without entering the unstable high-deflection regime observed in the fixed-flap sweep. No orbit loss was observed in the evaluated simulations; however, this demonstrates feasibility only for the prescribed cases and does not establish general closed-loop stability or robustness to turbulence, measurement uncertainty, or model mismatch. The simulator includes the stated

https://doi.org/10.5194/wes-2026-148
Preprint. Discussion started: 18 September 2026
© Author(s) 2026. CC BY 4.0 License.

surface-deflection limits and a first-order control-surface response, but Fig. 10 presents the commanded flap setpoint rather than an experimentally measured surface position. Verification of physical flap tracking, actuator loading, and the associated power improvement therefore remains necessary.

5.2 Trajectory geometry and wind-field sensitivity

The path-geometry results indicate that trajectory scale is more influential than the tested change in lateral path shape. Circular and elliptical trajectories produced similar average reel-out mechanical power under the considered conditions, whereas increasing the circular loop radius from 20 to $60\ \mathrm{m}$ reduced the average power from 8.98 to $6.99\ \mathrm{kW}$. Thus, for the present KM1 controller and operating conditions, the dominant geometric effect is associated with the scale of the orbit rather than with the difference between the tested circular and elliptical shapes.

The observed radius dependence is qualitatively consistent with the benefit of compact circular patterns discussed by Eijkelhof et al. (2026). However, their study identified a finite, system-specific preferred radius because the aerodynamic benefit of a smaller pattern is eventually offset by increased roll requirements, aircraft-speed constraints, and other operational limits. They also noted that potential wake losses, although not included in their simulations, could impose an additional limitation on very small patterns. Accordingly, the present result should be interpreted as a monotonic trend over the tested KM1 radius range and not as evidence that the smallest feasible radius is universally optimal. A direct quantitative comparison is not appropriate because Eijkelhof et al. considered the substantially larger MegAWES reference system, varied both flight-path and controller parameters, and evaluated full-cycle performance, whereas the present study retains fixed KM1 controller and hardware settings and evaluates average mechanical power during reel-out. Furthermore, the present circle–ellipse comparison does not constitute a direct comparison between circular and figure-of-eight patterns.

The wind-field cases reveal a separate sensitivity to the adopted inflow representation. Changing from the steady height-dependent profile with $v_1 = 9\ \mathrm{m\,s^{-1}}$ to the prescribed time-varying signal with $\bar{v}_1 = 8\ \mathrm{m\,s^{-1}}$, $A_v = 1\ \mathrm{m\,s^{-1}}$, and $T_v = 600\ \mathrm{s}$ reduced the average reel-out power from 8.36 to $7.56\ \mathrm{kW}$. Because these cases differ in both their mean reference wind speed and temporal structure, the observed difference cannot be attributed exclusively to wind unsteadiness. It instead demonstrates the conditional response of the simulated system to the combined change in mean inflow and temporal modulation. This comparison should not be interpreted as a general power penalty associated with unsteady wind because only one prescribed, deterministic signal was considered.

5.3 Operating height and elevation angle

Increasing the minimum production height shifts the traction trajectory towards a higher altitude band. Under the adopted logarithmic wind profile, this generally exposes the aircraft to higher wind speeds and dynamic pressure, thereby modifying the apparent wind, aerodynamic loading, tether tension, and winch response. At the same time, changing the operating height can alter the deployed tether length and the associated tether weight and aerodynamic drag. The best-performing range around 200–$220\ \mathrm{m}$, with an average reel-out power of $12.96\ \mathrm{kW}$ obtained near $200\ \mathrm{m}$, should therefore be interpreted as the combined response of the aircraft–tether–winch system rather than as an effect of wind speed alone.

https://doi.org/10.5194/wes-2026-148
Preprint. Discussion started: 18 September 2026
© Author(s) 2026. CC BY 4.0 License.

The minimum production height and helix-axis elevation angle do not modify the trajectory in identical ways. The minimum production height sets the lower boundary of the traction trajectory, whereas the elevation angle changes the inclination, altitude distribution, and flight kinematics of the helical path. After selecting the best-performing minimum height, the elevation-angle sweep produced its best result at the reference value $\theta_h = 10°$, equal to $12.96\,\mathrm{kW}$, and therefore provided no additional increase in average reel-out power.

The absence of an incremental improvement suggests that the two parameters have overlapping effects within the tested sequential optimization. Nevertheless, equal average-power values do not establish that the parameters are generally redundant, because the corresponding trajectories may differ in their instantaneous loads, power fluctuations, tracking behaviour, and operating margins. A coupled $(h_{\min}, \theta_h)$ sweep would be required to quantify their interaction and determine whether the sequentially identified setting is also a combined optimum.

5.4 Relation to previous AWES studies

The present findings are broadly consistent with previous work on KM1 modeling and traction-phase control, which emphasizes the coupling among aerodynamic loading, tether-force regulation, and crosswind guidance (Mohammed et al., 2024a, b; Rapp et al., 2019). In particular, the strong influence of aerodynamic actuation and sampled wind altitude agrees with the general understanding that practical AWES performance depends not only on wing aerodynamics, but also on how the controller maintains repeatable high-tension reel-out operation under varying inflow. A recent system-level comparison by Eijkelhof et al. (2026) found that, for the substantially larger MegAWES reference system, a circular pattern achieved the highest cycle-averaged power and required a smaller projected ground area, whereas the figure-of-eight down-loop provided lower power fluctuations and potentially lower cyclic loading. The present circle–ellipse comparison is narrower and evaluates average traction-phase power rather than net cycle power; it therefore complements, but does not directly reproduce, their circle–figure-of-eight comparison. Together, these findings show that flight-path selection must consider power output together with power quality, operational footprint, structural loading, and system-specific control constraints.

5.5 Limitations

The present results constitute a conditional sensitivity study for the KM1 configuration rather than a general optimization of ground-generation AWES operation. The controller structure, hardware limits, and non-investigated parameters were held fixed, and the one-factor-at-a-time design does not resolve interactions among flap scheduling, path geometry, operating height, and elevation angle. The reported best-performing values are therefore conditional on the selected baseline, controller, and parameter ranges. In particular, the matching minimum-height and elevation-angle results show that elevation-angle tuning provided no additional improvement in the sequential sweep, but they do not demonstrate general parameter redundancy.

The principal comparison metric is average mechanical power during reel-out. Although net pumping-cycle energy is defined in Eq. (29), the reported percentage improvements do not systematically account for changes in reel-out duration, retraction energy, transition time, total cycle duration, electrical-conversion losses, or auxiliary consumption. Consequently, an increase in average reel-out mechanical power does not necessarily produce an equal increase in net cycle energy, cycle-averaged

https://doi.org/10.5194/wes-2026-148
Preprint. Discussion started: 18 September 2026
© Author(s) 2026. CC BY 4.0 License.

electrical power, or annual energy production. Power quality, structural and fatigue loading, and operational footprint were also not included as optimization objectives.

The atmospheric inputs are limited to a logarithmic vertical profile and one prescribed deterministic time-varying ground-reference wind signal. These inputs do not represent the statistical variability of atmospheric turbulence, directional shear, spatial coherence, or transient gusts. In particular, extrapolating a neutral logarithmic profile with a single roughness length through the full 0–600 m range cannot reproduce stability effects, low-level jets, or the coastal internal boundary layers documented at Lista (Cheynet et al., 2025). Accordingly, the observed reduction in power under the time-varying case cannot be generalised as a power penalty associated with unsteady wind, and the reported absolute power levels should not be interpreted as site-specific energy-yield estimates.

The simulator applies the prescribed control-surface limits and a first-order control-surface response. Nevertheless, the scheduled-flap results have not been verified using experimentally measured flap positions or load-dependent actuator behaviour. Furthermore, although the underlying KM1 simulator has previously been assessed against flight data, the operating-parameter trends and predicted performance improvements reported in the present study have not been individually validated in flight. Future work should therefore consider coupled multi-objective optimization, broader atmospheric ensembles, full-cycle electrical-performance metrics, structural-loading measures, and experimental validation of the proposed operating strategies.

6 Conclusion

This study used a validated nonlinear kite–tether–winch simulator of the Kitemill KM1 rigid-wing ground-gen AWES ~~airborne wind energy system~~ to quantify how selected operating parameters affect reel-out mechanical power under variable wind conditions. Within the adopted baseline case, which combined an altitude-dependent wind profile with time-varying ground-reference wind input, the average reel-out power was 7.56 kW.

The results show that the dominant performance parameters for the investigated KM1 configuration are aerodynamic actuation and the altitude band sampled during traction. A speed-scheduled flap strategy increased the average reel-out power to 11.10 kW, corresponding to an improvement of approximately 47% relative to the baseline case, while repeated crosswind operation was maintained in the evaluated simulations. Optimizing the minimum production height further increased the average reel-out power to 12.96 kW, which is approximately 71% higher than the baseline value. By contrast, changes in lateral path shape had only a limited influence on average traction power under the tested conditions, whereas the scale of the trajectory, represented here by the circular loop radius, had a more pronounced effect. Elevation-angle tuning did not increase the reel-out power beyond the value obtained following minimum-height selection, suggesting an overlapping influence on the altitude distribution of the trajectory within the tested sequential optimization. A coupled parameter sweep would be required to establish the interaction between these parameters or demonstrate general redundancy.

Taken together, these findings indicate that, for the investigated KM1 system and controller configuration, improvements in reel-out performance are achieved more effectively through flap scheduling and operating-height selection than through modest changes in lateral path shape. At the same time, the reported values should be interpreted within the scope of the present study.

https://doi.org/10.5194/wes-2026-148
Preprint. Discussion started: 18 September 2026
© Author(s) 2026. CC BY 4.0 License.

The conclusions are specific to the KM1 model, the adopted controller structure, and the evaluated simulation conditions, and they are based on reel-out mechanical power at the ground-station drum rather than on full net-cycle electrical output. Future work should therefore examine coupled optimization of the operating parameters, include broader atmospheric variability and turbulence representations, and compare the simulation-based trends against additional experimental or flight-test data.

https://doi.org/10.5194/wes-2026-148
Preprint. Discussion started: 18 September 2026
© Author(s) 2026. CC BY 4.0 License.

Appendix A: Study-specific KM1 parameters and implementation details

The nonlinear kite–tether–winch model used in this study is the KM1 simulation framework described by Mohammed et al. (2024a). That publication provides the complete rigid-body equations, lumped-mass tether formulation, aerodynamic coefficient fits, model parameters, and validation against flight data. These previously published derivations and coefficient plots are therefore not repeated here.

This appendix collects only the KM1 platform parameters, operating limits, and study-specific settings required to interpret the present simulation campaign. The VTOL configuration and associated rotor model are not part of the operating-parameter analysis reported in this paper and have consequently been omitted.

A1 KM1 platform and ground-station parameters

The principal aircraft and ground-station parameters used in the simulations are summarized in Table A1. These values are retained here because they define the physical scale and operating envelope of the investigated KM1 configuration.

Table A1. KM1 aircraft and ground-station parameters used in the present study (Mohammed et al., 2024a).

Parameter and symbol	Value	Unit
Aircraft mass m_a	54	kg
Aircraft inertia $J_{xx}, J_{yy}, J_{zz}, J_{xz}$	33.70, 23.75, 66.33, 3.00	kg m^2
Wing area S	2.982	m^2
Wingspan b	7.4	m
Mean aerodynamic chord $\bar{c}$	0.431	m
Maximum winch mechanical power $P_w^{\max}$	35	kW
Maximum tether force $F_{\max}$	7500	N

A2 Actuator, winch, and tether limits

Table A2 lists the actuator, winch, and tether limits applied throughout the simulation campaign. These limits were held fixed so that differences between cases could be attributed to the investigated operating parameters rather than to changes in hardware capability.

A3 Reference and study-specific settings

The reference operating condition and the numerical settings introduced specifically for the present parameter study are summarized in Table A3. The corresponding definitions and simulation results are presented in Sects. 3 and 4.

https://doi.org/10.5194/wes-2026-148
Preprint. Discussion started: 18 September 2026
© Author(s) 2026. CC BY 4.0 License.

Table A2. KM1 actuator, winch, and tether limits used in the present study (Mohammed et al., 2024a).

Parameter and symbol	Value	Unit
Maximum tether length $\ell_{t,\max}$	600	m
Aileron limits $[\delta_{a,\min}, \delta_{a,\max}]$	$[-10,\ 10]$	deg
Elevator limits $[\delta_{e,\min}, \delta_{e,\max}]$	$[-16,\ 16]$	deg
Rudder limits $[\delta_{r,\min}, \delta_{r,\max}]$	$[-20,\ 20]$	deg
Control-surface time constant τ_s	0.015	s
Winch-speed limits $[v_{t,\min}, v_{t,\max}]$	$[-20,\ 20]$	$\mathrm{m\,s^{-1}}$
Winch time constant τ_w	0.3	s
Tether breaking-load rating $\bar{F}_t$	1184	kg
Tether elongation at breaking load $\bar{\epsilon}_t$	2.9	%

Table A3. Reference and study-specific settings used in the simulation campaign.

Setting and symbol	Value	Unit
Reference minimum production height $h_{\min}$	150	m
Reference helix-axis elevation angle θ_h	10	deg
Reference flap deflection δ_f	5	deg
Uniform freestream wind speed	12	$\mathrm{m\,s^{-1}}$
Wind-profile reference height h_1	10	m
Wind-profile reference speed v_1	9	$\mathrm{m\,s^{-1}}$
Terrain roughness length z_0	0.03	m
Scheduled flap-command range $[\delta_{f,\mathrm{cmd},\min}, \delta_{f,\mathrm{cmd},\max}]$	$[0,\ 10]$	deg

A4 Use of the published aerodynamic model

The aerodynamic force and moment coefficients used in the simulator are evaluated using the CFD-based KM1 coefficient functions reported by Mohammed et al. (2024a). No new aerodynamic coefficients were identified or fitted in the present study. Instead, the existing model was evaluated under different flap commands, path geometries, wind-field representations, minimum production heights, and helix-axis elevation angles.

Because the complete coefficient equations, numerical coefficient values, and supporting coefficient plots are already available in the cited publication, reproducing them here would duplicate previously published material without adding information specific to the present analysis. The compact coefficient relations retained in Sect. 2.4 are sufficient to show how flap deflection and the other control-surface inputs enter the aerodynamic model.

https://doi.org/10.5194/wes-2026-148
Preprint. Discussion started: 18 September 2026
© Author(s) 2026. CC BY 4.0 License.

Funding

This work was supported by the United Arab Emirates University under Grant 12R230.

Data availability. Data supporting the conclusions of this article will be made available upon reasonable request from the corresponding author.

Author contributions. Pritti Paul: conceptualization, methodology, software, formal analysis, investigation, data curation, visualization, and writing – original draft. Yahya Khurshid: investigation, formal analysis, literature review, and writing — review and editing. Espen Oland: conceptualization, methodology, supervision, and writing – review and editing. Mohamed M. Kamra: methodology, validation, formal analysis, and writing – review and editing. Tarek N. Dief: conceptualization, supervision, project administration, and writing — review and editing.

Competing interests. The authors declare that they have no known competing financial interests or personal relationships that could have appeared to influence the work reported in this paper.

Disclaimer. The authors acknowledge the use of generative artificial intelligence and AI-assisted tools during the preparation of this manuscript to support language editing, clarity, and stylistic refinement. All technical content, analyses, interpretations, and conclusions were developed and verified by the authors.

Acknowledgements. The authors would like to thank Kitemill AS for providing access to the KM1 reference model and the associated high-fidelity nonlinear MATLAB/Simulink simulator, as well as for insightful discussions on airborne wind energy system modeling and control.

https://doi.org/10.5194/wes-2026-148
Preprint. Discussion started: 18 September 2026
© Author(s) 2026. CC BY 4.0 License.

References

~~Bošnjaković, M., Santa, R., Topić Božić, J., and Muhić, S.: The Future of Vertical Axis Wind Turbines: Opportunities, Challenges, and Sustainability Perspectives, Energies, 18, 6369, https://doi.org/10.3390/en18236369, 2025.~~

Cheynet, E., Diezel, J. M., Haakenstad, H., Breivik, Ø., Peña, A., and Reuder, J.: Tall wind profile validation of ERA5, NORA3, and NEWA datasets using lidar observations, Wind Energy Science, 10, 733–754, https://doi.org/10.5194/wes-10-733-2025, 2025.

Crismer, J.-B., Haas, T., Duponcheel, M., and Winckelmans, G.: Airborne wind energy systems flying optimal trajectories in turbulent wind using flight path tracking, in: Journal of Physics: Conference Series, vol. 2767, p. 072021, IOP Publishing, https://doi.org/10.1088/1742-6596/2767/7/072021, 2024.

Eijkelhof, D. and Schmehl, R.: Six-degrees-of-freedom simulation model for future multi-megawatt airborne wind energy systems, Renewable Energy, 196, 137–150, https://doi.org/https://doi.org/10.1016/j.renene.2022.06.094, 2022.

Eijkelhof, D., Rossi, N., and Schmehl, R.: Optimal flight pattern debate for airborne wind energy systems: circular or figure of eight?, Wind Energy Science, 11, 1287–1304, https://doi.org/10.5194/wes-11-1287-2026, 2026.

Fagiano, L., Nguyen-Van, E., Rager, F., Schnez, S., and Ohler, C.: Autonomous Takeoff and Flight of a Tethered Aircraft for Airborne Wind Energy, IEEE Transactions on Control Systems Technology, 26, 151–166, https://doi.org/10.1109/TCST.2017.2661825, 2018.

Fagiano, L., Quack, M., Bauer, F., Carnel, L., and Oland, E.: Autonomous airborne wind energy systems: accomplishments and challenges, Annual Review of Control, Robotics, and Autonomous Systems, 5, 603–631, https://doi.org/https://doi.org/10.1146/annurev-control-042820-124658, 2022.

Joshi, R., Schmehl, R., and Kruijff, M.: Power curve modelling and scaling of fixed-wing ground-generation airborne wind energy systems, Wind Energy Science, 9, 2195–2215, https://doi.org/10.5194/wes-9-2195-2024, 2024.

Joshi, R., von Terzi, D., and Schmehl, R.: System design and scaling trends in airborne wind energy demonstrated for a ground-generation concept, Wind Energy Science, 10, 695–718, https://doi.org/10.5194/wes-10-695-2025, 2025.

Khurshid, Y., Paul, P., Elhesasy, M., Ali, B., Kamra, M. M., Okasha, M., and Dief, T. N.: From inception to commercialization: A systematic review of airborne wind energy systems, Sustainable Energy Technologies and Assessments, 83, 104 623, https://doi.org/10.1016/j.seta.2025.104623, 2025.

Loyd, M. L.: Crosswind kite power (for large-scale wind power production), Journal of energy, 4, 106–111, https://doi.org/https://doi.org/10.2514/3.48021, 1980.

Malz, E. C., Walter, V., Göransson, L., and Gros, S.: The value of airborne wind energy to the electricity system, Wind Energy, 25, 281–299, https://doi.org/DOI10.1002/we.2671, 2022.

Marques, M. N., Magalhães, S. A., Dos Santos, F. N., and Mendonça, H. S.: Tethered Unmanned Aerial Vehicles—A Systematic Review, Robotics, 12, https://doi.org/10.3390/robotics12040117, 2023.

Mohammed, T., Busk, J., Oland, E., and Fagiano, L.: Large-Scale Reverse Pumping for Rigid-Wing Airborne Wind Energy Systems, Journal of Guidance, Control, and Dynamics, 47, 1748–1758, https://doi.org/10.2514/1.G007859, 2024a.

Mohammed, T., Oland, E., and Fagiano, L.: Fault Tolerant Flight Control for the Traction Phase of Pumping Airborne Wind Energy Systems, International Journal of Control, Automation and Systems, 22, 2428–2443, https://doi.org/10.1007/s12555-023-0588-z, 2024b.

Onay, A. E., Dokur, E., and Kurban, M.: Comparative Life Cycle Assessment of Airborne Wind Energy and Horizontal Axis Wind Turbines in Türkiye, in: 2023 4th International Conference on Communications, Information, Electronic and Energy Systems (CIEES), pp. 1–4, https://doi.org/10.1109/CIEES58940.2023.10378841, 2023.

https://doi.org/10.5194/wes-2026-148
Preprint. Discussion started: 18 September 2026
© Author(s) 2026. CC BY 4.0 License.

Rapp, S., Schmehl, R., Oland, E., and Haas, T.: Cascaded pumping cycle control for rigid wing airborne wind energy systems, Journal of Guidance, Control, and Dynamics, 42, 2456–2473, https://doi.org/https://doi.org/10.2514/1.G004246, 2019.

Sommerfeld, M., Dörenkämper, M., De Schutter, J., and Crawford, C.: Impact of wind profiles on ground-generation airborne wind energy system performance, Wind Energy Science, 8, 1153–1178, https://doi.org/10.5194/wes-8-1153-2023, 2023.

Vermillion, C., Cobb, M., Fagiano, L., Leuthold, R., Diehl, M., Smith, R. S., Wood, T. A., Rapp, S., Schmehl, R., Olinger, D., and Demetriou, M.: Electricity in the air: Insights from two decades of advanced control research and experimental flight testing of airborne wind energy systems, Annual Reviews in Control, 52, 330–357, https://doi.org/https://doi.org/10.1016/j.arcontrol.2021.03.002, 2021.

Weber, J., Marquis, M., Cooperman, A., Draxl, C., Hammond, R., Jonkman, J., Lemke, A., Lopez, A., Mudafort, R., Optis, M., et al.: Airborne Wind Energy, Tech. rep., National Renewable Energy Laboratory (NREL), Golden, CO (United States), https://doi.org/10.2172/1778246, 2021.